bioRxiv preprint doi: https://doi.org/10.1101/279505; this version posted November 15, 2018. The copyright holder for this preprint (which was not certified by peer review) is the author/funder. All rights reserved. No reuse allowed without permission.

Dendritic NMDA receptors in parvalbumin neurons enable strong and stable neuronal assemblies

Jonathan Cornford[1], Marion S Mercier[1]†, Marco Leite[1]†, Vincent Magloire[1], Michael Häusser[2], Dimitri M Kullmann[1*]

Affiliations:

[1]UCL Institute of Neurology, University College London,

[2]Wolfson Institute for Biomedical Research, University College London,

*Correspondence to: d.kullmann@ucl.ac.uk

†These authors contributed equally

Abstract: Fast-spiking, parvalbumin-expressing (PV+) GABAergic interneurons mediate feedforward and feedback inhibition and have a key role in gamma oscillations and information processing. The importance of fast PV+ cell signalling for these circuit functions is well established. In contrast, the adaptive significance of NMDA receptors (NMDARs), which generate relatively slow postsynaptic currents, in PV+ cells is unclear. Underlining their potential importance, several studies implicate PV+ cell NMDAR disruption in pathology and impaired network function. Here, we show that NMDARs underlie supralinear integration of feedback excitation from local pyramidal neurons onto mouse CA1 PV+ cells. Furthermore, by incorporating NMDARs at feedback connections onto PV+ cells in spiking neural networks, we show that these receptors enable cooperative recruitment of PV+ interneurons, strengthening and stabilising principal cell assemblies. Failure of this phenomenon provides a parsimonious explanation for cognitive and sensory gating deficits in pathologies with impaired PV+ NMDAR signalling.

bioRxiv preprint doi: https://doi.org/10.1101/279505; this version posted November 15, 2018. The copyright holder for this preprint (which was not certified by peer review) is the author/funder. All rights reserved. No reuse allowed without permission.

Introduction

Interactions among cell assemblies underlie information representation and processing in the brain (Buzsáki, 2010). Inhibitory interneurons, including fast-spiking PV+ cells, which mediate feedforward and feedback inhibition and are central to gamma oscillations, have a major role in segregating excitatory principal cells into functional groups. PV+ cells have broad receptive fields inherited from multiple converging heterogeneously tuned principal neurons (Kerlin et al., 2010), and coupled with their powerful somatic inhibition of principal cells, they are positioned to mediate a "winner-takes-all" scheme in which assemblies inhibit each other (Agetsuma et al., 2018; Trouche et al., 2016).

The biophysical properties of PV+ cells that make them suited to fast inhibition of target neurons are well established (Jonas et al., 2004). These properties are critical for functions such as the enforcement of narrow temporal integration, input normalization, and sparsification of "winning" assemblies (de Almeida et al., 2009; Pouille and Scanziani, 2001; Pouille et al., 2009). However, PV+ interneurons are also equipped with NMDA receptors (NMDARs) whose slow kinetics and nonlinear voltage dependence do not appear well-aligned with fast inhibition of principal cells. Although NMDARs contribute relatively less to synaptic excitation of PV+ cells than principal neurons (Lamsa *et al.*, 2007; Matta *et al.*, 2013), several sources of evidence suggest that they are important for the normal operation of cell assemblies. Thus, genetic deletion of NMDARs in PV+ interneurons disrupts both gamma rhythms (Carlén et al., 2012) and spatial representations (Korotkova et al., 2010). Moreover, impaired NMDAR-mediated signalling in PV+ interneurons has been suggested to be a core feature of schizophrenia (Coyle, 2012; Lisman et al., 2008). Indeed, genetic manipulation of the schizophrenia risk genes encoding neuregulin and ErbB4, which regulate NMDARs, impairs recruitment of PV+ interneurons (delPino et al., 2013; Kotzadimitriou et al., 2018) and recapitulates some features of the disease.

Although PV+ interneurons in the hippocampal CA1 field have relatively small NMDAR-mediated currents (Lamsa *et al.*, 2007; Matta *et al.*, 2013), a recent study reported that NMDARs contribute more to synaptic excitation at feedback synapses from local pyramidal neurons than at feedforward connections made by Schaffer collaterals (Le Roux et al., 2013). Feedback connections onto interneurons and

bioRxiv preprint doi: https://doi.org/10.1101/279505; this version posted November 15, 2018. The copyright holder for this preprint (which was not certified by peer review) is the author/funder. All rights reserved. No reuse allowed without permission.

recurrent inhibition constitute the inhibitory microcircuit motifs that underlie cell assembly competition. In principal neurons, NMDAR-mediated dendritic nonlinearities enhance the computing capacity of individual cells (Gasparini, 2006; Losonczy and Magee, 2006; Poirazi and Mel, 2001; Stuart and Spruston, 2015). We therefore asked if NMDARs have an analogous function in PV+ interneurons and whether dendritic coincidence detection could have an important role in competition among cell assemblies.

Here we combine *in vitro* optogenetic stimulation and two-photon glutamate uncaging with modelling to assess the role of NMDARs at excitatory feedback connections onto mouse hippocampal CA1 PV+ interneurons. We show that NMDARs at feedback synapses mediate integrative dendritic nonlinearities in PV+ interneurons. Importantly, this mechanism can be exploited to promote the formation of robust cell assemblies that are stable in the face of distracting noise.

bioRxiv preprint doi: https://doi.org/10.1101/279505; this version posted November 15, 2018. The copyright holder for this preprint (which was not certified by peer review) is the author/funder. All rights reserved. No reuse allowed without permission.

Results

NMDARs recruitment at CA1 pyramidal cell feedback connections onto PV+ interneurons.

PV+ interneurons in hippocampal CA1 with cell bodies in stratum pyramidale comprise basket and axo-axonic cells, and receive excitatory feedforward inputs distributed throughout their dendritic trees, in both strata radiatum and oriens. They are also innervated by axon collaterals of local pyramidal cells, although these synapses are confined to dendrites in the stratum oriens (Amaral et al., 1991). Extracellular stimulation in stratum radiatum therefore evokes feedforward excitation of PV+ interneurons, while feedback inputs from CA1 pyramidal cells are activated by stimulating in the alveus. Existing evidence that feedback connections exhibit a higher NMDAR/AMPAR conductance ratio than Schaffer collateral feedforward synapses (Le Roux et al., 2013) was obtained by simulating in the alveus or stratum radiatum respectively, while voltage clamping PV+ interneurons at positive and negative potentials to separate the two components of excitatory transmission. However, the low input resistance of PV+ interneurons, together with different dendritic morphologies in strata oriens and radiatum (Hu et al., 2010), potentially confound the measurement of excitatory postsynaptic currents (EPSCs) recorded at positive holding potentials (Williams and Mitchell, 2008). We therefore complemented these experiments by recording EPSCs in a low (0.1 mM) extracellular [Mg^{2+}] solution to partially unblock NMDARs while holding PV+ interneurons at –60 mV, and using sequential addition of AMPAR and NMDAR blockers to separate the two components of transmission (**Figure 1A**). Experiments were performed in acute hippocampal slices from mice obtained by crossing PV-cre mice with Ai9 mice, and tdTomato expression was used to target fast-spiking PV+ interneurons in stratum pyramidale.

Pharmacological dissection of EPSCs in 0.1 mM [Mg^{2+}] revealed a >2-fold greater NMDAR/AMPAR charge ratio when stimulating in the alveus to antidromically excite feedback axons of local pyramidal neurons (Pouille and Scanziani, 2004) than when stimulating in stratum radiatum to excite feedforward Schaffer collaterals (charge ratio: 3.5 ± 0.7 vs 1.3 ± 0.3, P = 0.0017, n = 10, paired t-test; **Figure 1A**).

bioRxiv preprint doi: https://doi.org/10.1101/279505; this version posted November 15, 2018. The copyright holder for this preprint (which was not certified by peer review) is the author/funder. All rights reserved. No reuse allowed without permission.

This dataset complements the previous evidence for a greater contribution of NMDARs at feedback synapses. Nevertheless, it is also possible that, in addition to recruiting feedback collaterals, extracellular stimulation in the alveus recruits a population of extrinsic afferents that activate NMDARs on PV+ cells. We therefore performed paired recordings and found that evoked action potentials in pyramidal cells elicited monosynaptic currents in PV+ cells with a detectable NMDAR component in 3 out of 5 connections (5/31 potential pairs tested were connected; **Figure 1B**), confirming the presence of an NMDAR component at least at some local feedback excitatory synapses.

In order to investigate the role of NMDARs in synaptic integration of feedback connections, we turned to an optogenetic strategy. ChR2 was selectively expressed in CA1 pyramidal cells by injecting an adeno-associated virus (AAV) encoding ChR2-EYFP under the control of the CaMKII promoter in the dorsal hippocampus. We verified that expression was confined to CA1 and did not spread to CA3 (**Figure 1C**). Wide-field illumination pulses (1ms) of 470 nm light elicited monosynaptic excitatory postsynaptic potentials (EPSPs), in agreement with the low associative connectivity among CA1 pyramidal neurons (Amaral et al., 1991; Deuchars and Thomson, 1996) (**Figure 1D**). Perfusion of the NMDAR blocker D-AP5 significantly reduced both the average EPSP time-integral and the peak-amplitude normalized EPSP integral (P = 0.033; P = 0.014; n=5) (**Figures 1D and 1E**). Furthermore, in line with cooperative postsynaptic voltage-dependent relief of Mg^{2+} blockade, we observed a larger NMDAR contribution to EPSPs elicited by stronger light pulses (**Figure 1F**).

bioRxiv preprint doi: https://doi.org/10.1101/279505; this version posted November 15, 2018. The copyright holder for this preprint (which was not certified by peer review) is the author/funder. All rights reserved. No reuse allowed without permission.

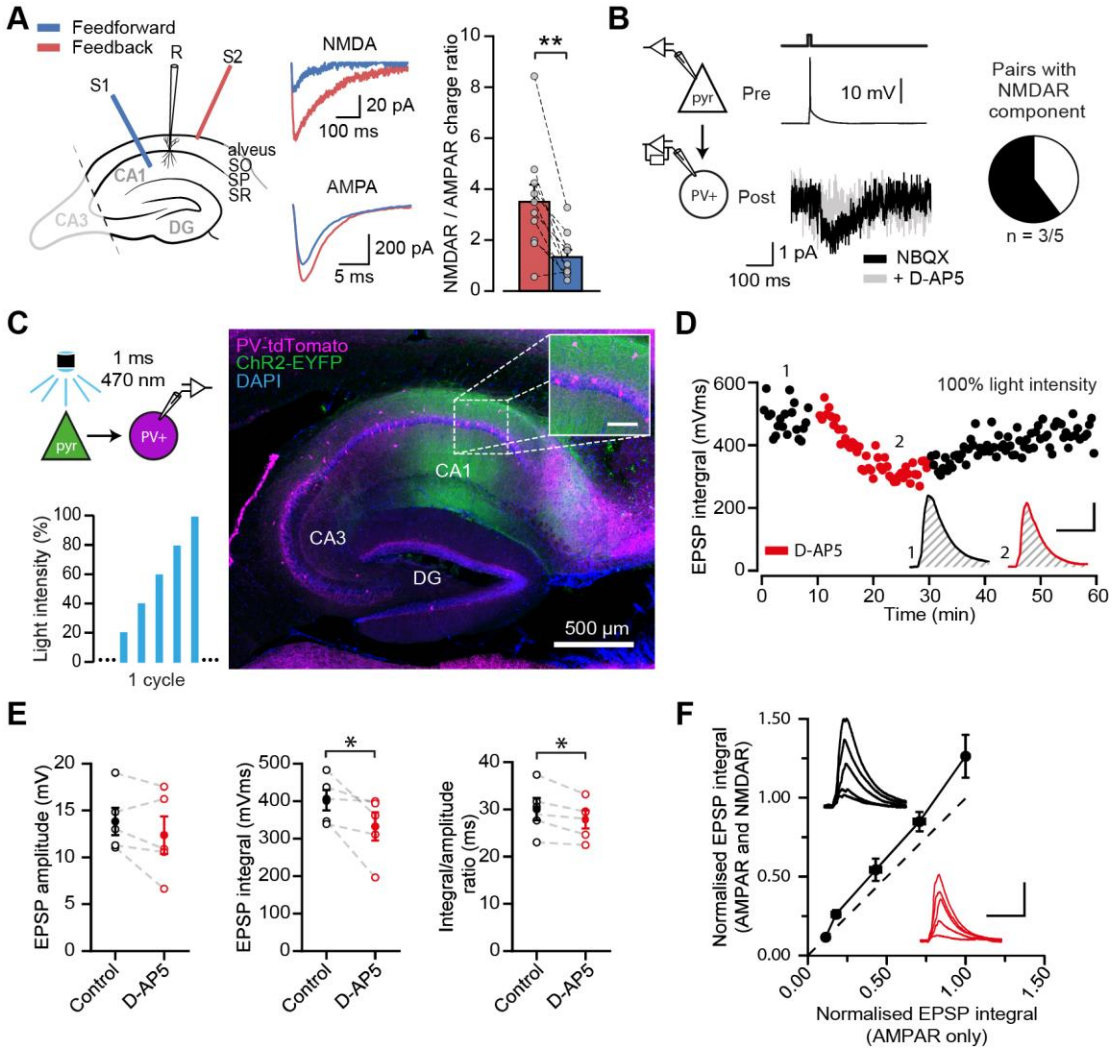

Figure 1. NMDAR recruitment at CA1 pyramidal cell feedback connections onto PV+ interneurons.

(A) Schematic describing stimulation of feedforward (S1, blue) and antidromic stimulation of feedback (S2, red) connections. Middle: example paired AMPAR and NMDAR EPSC components in low [Mg^{2+}]. Right: NMDAR/AMPAR charge ratios (n = 10).

(B) Experimental setup (left) and example traces (right) of paired CA1 pyramidal cell – PV+ interneuron recordings, in low [Mg^{2+}]. 3 of 5 connected pairs had a detectable NMDAR component.

(C) Optogenetic stimulation of CA1 pyramidal cells was used to evoke population feedback EPSPs in PV+ interneurons (top left). Light power was cycled from 20% to 100% of power for maximal response (see methods, bottom left). Example image

bioRxiv preprint doi: https://doi.org/10.1101/279505; this version posted November 15, 2018. The copyright holder for this preprint (which was not certified by peer review) is the author/funder. All rights reserved. No reuse allowed without permission.

showing ChR2-EYFP under the CaMKII promoter injected into the CA1 region of PV-tdTomato mice (right; inset scale: 100 µm).

(D) EPSP integral of maximal response over time, with 20 min application of D-AP5 (scale: 5 mV, 50 ms).

(E) EPSP amplitude, EPSP integral and integral/amplitude ratio in the presence (red) or absence (black) of D-AP5 (n = 5, one-tailed *t*-tests; control = average of baseline and wash). Filled circles and error bars indicate mean ± SEM.

(F) Normalised EPSP integrals (black example traces) vs normalised EPSP integrals in the presence of D-AP5 (red example traces), for all stimulation intensities (n = 5; scale: 5 mV, 50 ms).

Differential input integration at stratum oriens and stratum radiatum dendrites of PV+ interneurons.

To understand how NMDARs contribute to dendritic integration in PV+ interneurons, we recorded somatic responses to two-photon glutamate uncaging at multiple sites within a 15 µm dendritic segment in either stratum oriens or stratum radiatum (**Figure 2A**). Activation of individual uncaging locations produced uncaging-evoked EPSPs (uEPSPs) that were comparable in amplitude and kinetics to spontaneous EPSPs (**Figure 2B** and Figure S1), consistent with a high density of excitatory synapses innervating PV+ interneuron dendrites (Gulyás et al., 1999). To quantify the degree of nonlinearity of dendritic integration, we compared compound uEPSPs elicited by near-synchronous activation of increasing numbers of uncaging locations to the arithmetic sum of individual uEPSPs at the same sites (**Figure 2C**). Activation of sites on dendrites in stratum oriens revealed supralinear uEPSP summation (peak amplitude nonlinearity: 24.0 ± 4.5%, mean ± SEM, n = 14; **Figures 2D and 2E**; unscaled responses in Figure S2). This nonlinearity was even larger when measured using the time-integral of uEPSPs (time-integral nonlinearity from 0 to 50 ms: 54.0 ± 10.1%; **Figure 2F**). In contrast, when glutamate was uncaged along dendritic segments in stratum radiatum, uEPSPs summated in a linear fashion (peak amplitude nonlinearity: 3.8 ± 5.0%, time-integral nonlinearity: 6.3 ± 7.6%, n = 9; oriens vs. radiatum P = 0.0083 and P = 0.0028 for peak amplitude and time-integral comparisons respectively, unpaired *t*-tests, **Figures 2D–2F**). The difference between strata was also observed in a subset of paired recordings in which both dendrites were tested (Figure S3). There was no significant relationship between integration

bioRxiv preprint doi: https://doi.org/10.1101/279505; this version posted November 15, 2018. The copyright holder for this preprint (which was not certified by peer review) is the author/funder. All rights reserved. No reuse allowed without permission.

nonlinearity and either uncaging distance from soma or the size of the arithmetic sum of the uEPSPs (Figure S4).

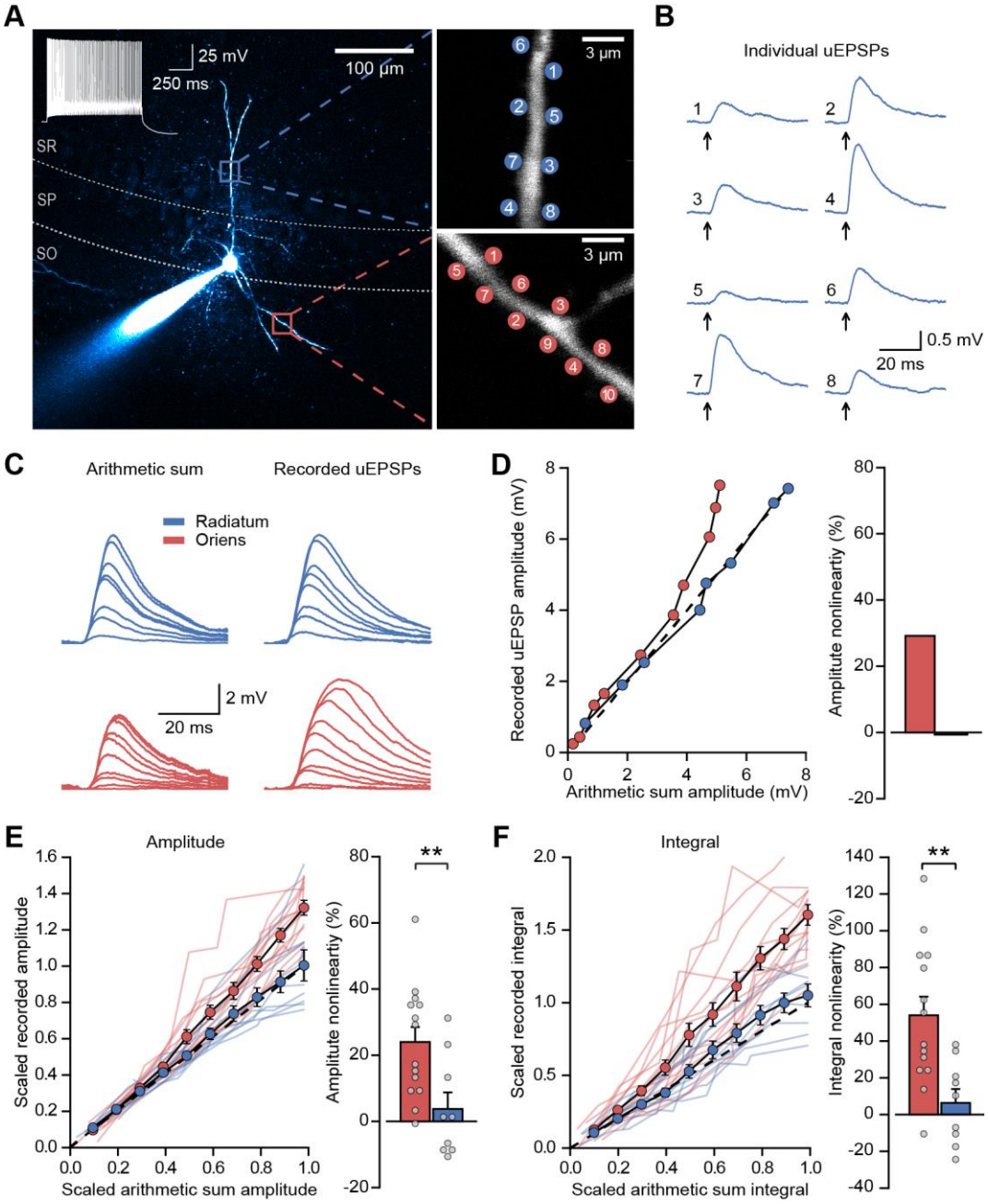

Figure 2. Differential input integration at stratum oriens and stratum radiatum dendrites of PV+ interneurons.

(A) Two-photon z-projection image of a PV+ interneuron recorded via a patch pipette in stratum pyramidale (SP) and filled with Alexa-594 (left), with two dendritic

bioRxiv preprint doi: https://doi.org/10.1101/279505; this version posted November 15, 2018. The copyright holder for this preprint (which was not certified by peer review) is the author/funder. All rights reserved. No reuse allowed without permission.

regions of interest at higher magnification (right: top, stratum radiatum, SR; bottom, stratum oriens, SO), showing glutamate uncaging locations (numbered).

(B) Individual uEPSP responses from radiatum dendritic locations shown in (A).

(C) Comparison of arithmetic sum of individual uEPSPs and recorded uEPSPs evoked by near-synchronous uncaging at multiple locations in stratum radiatum (blue) and oriens (red).

(D) Peak amplitudes of recorded uEPSPs plotted against arithmetically summed waveforms for the two regions shown in (A). Dashed line shows line of identity. Right: bar chart showing percentage amplitude nonlinearity. Red: oriens, blue: radiatum.

(E) Summary of scaled peak amplitude comparisons for all cells (oriens locations: n = 14, radiatum locations: n = 9). Filled circles and error bars indicate mean ± SEM. Right: bar chart showing quantification of amplitude nonlinearity.

(F) Time-integral nonlinearity plotted as for (E). **: $p < 0.01$.

NMDAR expression and dendrite morphology underlie stratum-dependent differences in synaptic integration.

In line with the evidence for an NMDAR component at feedback inputs onto PV+ cells (Le Roux et al., 2013) (**Figure 1**), supralinear dendritic summation in stratum oriens was abolished when NMDARs were blocked by D-AP5 (time-integral nonlinearity: 2.5 ± 3.0 %, vs control $P = 0.0004$, n = 10; **Figures 3A–3C**). Dendritic integration in stratum radiatum was unchanged from control conditions (time-integral nonlinearity: 3.3 ± 2.6 %, vs control $P = 0.88$, n = 4; **Figures 3A–3C**). In contrast to D-AP5, the sodium channel blocker tetrodotoxin (TTX, 100 nM) did not significantly affect integration in either stratum oriens or radiatum (oriens time-integral nonlinearity 40.1 ± 5.6 %, vs control $P = 0.23$, n = 16; radiatum time-integral nonlinearity 9.4 ± 3.3 %, vs control $P = 0.71$, n = 9; **Figure 3D**). The failure of TTX to affect uEPSP integration is consistent with the view that PV+ interneuron dendrites generally do not support regenerative events (Hu et al., 2010) (although see (Chiovini et al., 2014)). The effects of pharmacological manipulations were consistent whether measuring peak uEPSP amplitudes or time-integrals (Figure S5). Furthermore, uncaging distances from soma were comparable across all conditions, as were somatic uEPSP amplitudes (Figure S6). Dendrites of PV+ interneurons mediating feedback inhibition, but not feedforward inhibition, thus exhibit supralinear input integration,

bioRxiv preprint doi: https://doi.org/10.1101/279505; this version posted November 15, 2018. The copyright holder for this preprint (which was not certified by peer review) is the author/funder. All rights reserved. No reuse allowed without permission.

most likely mediated by clusters of coactive synapses engaging depolarization-dependent relief of NMDARs from Mg^{2+} blockade.

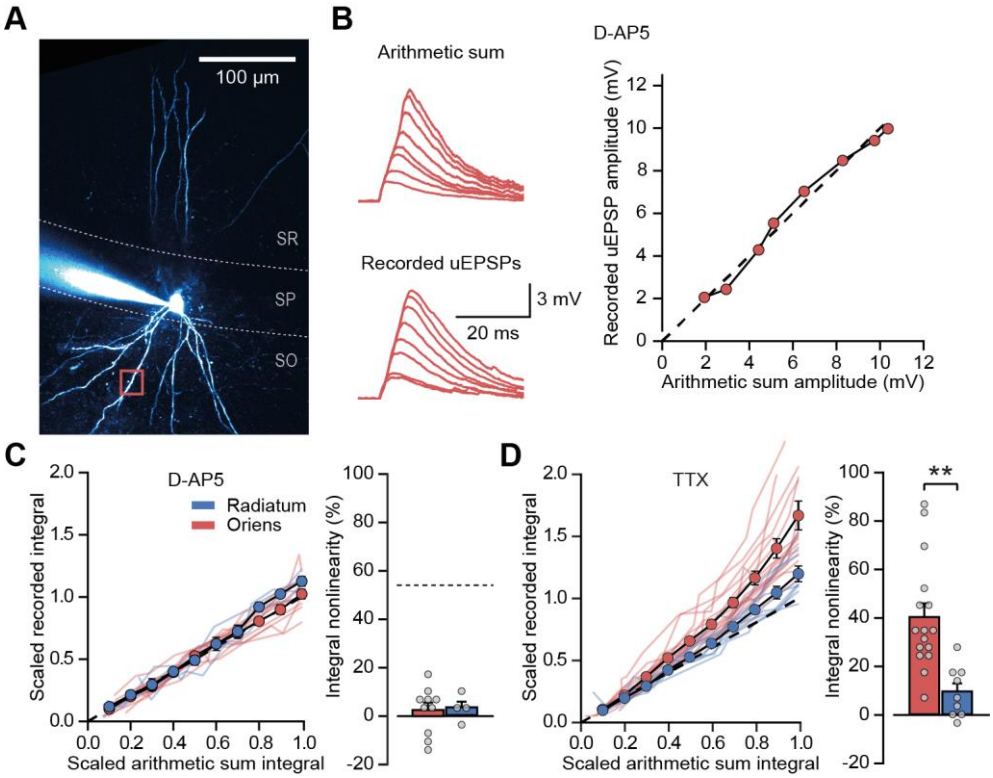

Figure 3. NMDARs mediate stratum oriens dendrite synaptic integration supralinearity.

(A) Two-photon z-stack of PV+ interneuron in CA1 region of hippocampus. Red box marks glutamate uncaging location.

(B) Comparison of arithmetic and recorded uEPSP summation waveforms in the presence of D-AP5. Right: peak recorded amplitude vs peak arithmetic amplitude.

(C) Summary data of time-integrals plotted against arithmetic sum time-integrals for 14 dendritic locations recorded in D-AP5 (oriens locations: n = 10, radiatum locations: n = 4). Right: quantified synaptic integration nonlinearity. The dashed line marks the average magnitude of oriens nonlinearity from Figure 1F.

(D) Summary data for 25 dendritic locations recorded in TTX (oriens locations: n = 16, radiatum locations: n = 9). Right: quantification of synaptic integration nonlinearity. Filled circles and error bars indicate mean ± SEM.

bioRxiv preprint doi: https://doi.org/10.1101/279505; this version posted November 15, 2018. The copyright holder for this preprint (which was not certified by peer review) is the author/funder. All rights reserved. No reuse allowed without permission.

Although the data summarized above can be explained by oriens dendrites of PV+ interneurons receiving synapses with enriched NMDAR content, they are generally thinner and shorter than those in stratum radiatum (Gulyás et al., 1999). This raises the possibility that oriens dendrites are depolarized more effectively by glutamate uncaging acting on AMPARs, because of a higher effective local input impedance, thereby enhancing relief of NMDARs from voltage-dependent block by Mg^{2+} (Branco et al., 2010). To investigate the relationship between synaptic integration and dendritic geometry we used a detailed compartmental model of a CA1 PV+ interneuron (**Figure 4A**). Voltage-dependent conductance densities and membrane properties were implemented according to previously published models (Hu and Jonas, 2014; Nörenberg et al., 2010), and the relative densities of synaptic AMPARs and NMDARs were initially assumed to be the same on oriens and radiatum dendrites. Simulation parameters closely followed the uncaging experiments, with clusters of synapses activated across the range of experimentally measured locations. These simulations revealed supralinear summation of EPSPs recorded at the soma that was more pronounced for stratum oriens than for stratum radiatum dendrites (oriens vs radiatum time-integral nonlinearity: 42.5 ± 3.5 % vs 23.9 ± 2.3 *%*, $P = 0.0005$, **Figure 4B**), supporting a role for dendritic morphology in mediating the difference between strata. The simulation results were very similar whether AMPARs were assumed to show polyamine-dependent inward rectification or to have a fixed open-channel conductance (Figure S7). The ~ 2-fold difference between strata was, however, smaller than the >8-fold difference observed experimentally (oriens vs radiatum time-integral nonlinearity: 54.0 ± 10.1 % vs 6.3 ± 7.6 %; **Figure 2**).

Reducing the simulated NMDAR/AMPAR conductance ratio at radiatum dendrites to half that of the oriens dendrites, in line with results from experiments shown in **Figure 1**, improved agreement with the glutamate uncaging data (time-integral supralinearity in simulations: 42.5 ± 3.5 % vs 8.5 ± 0.8 % for stratum oriens vs stratum radiatum; **Figure 4C**). The striking difference in dendritic integration in oriens and radiatum dendrites observed experimentally (**Figure 2**) can therefore be accounted for by a combination of differential NMDAR expression (greater in stratum oriens) and dendritic morphology (greater impedance in stratum oriens, thus facilitating depolarization and NMDAR opening).

bioRxiv preprint doi: https://doi.org/10.1101/279505; this version posted November 15, 2018. The copyright holder for this preprint (which was not certified by peer review) is the author/funder. All rights reserved. No reuse allowed without permission.

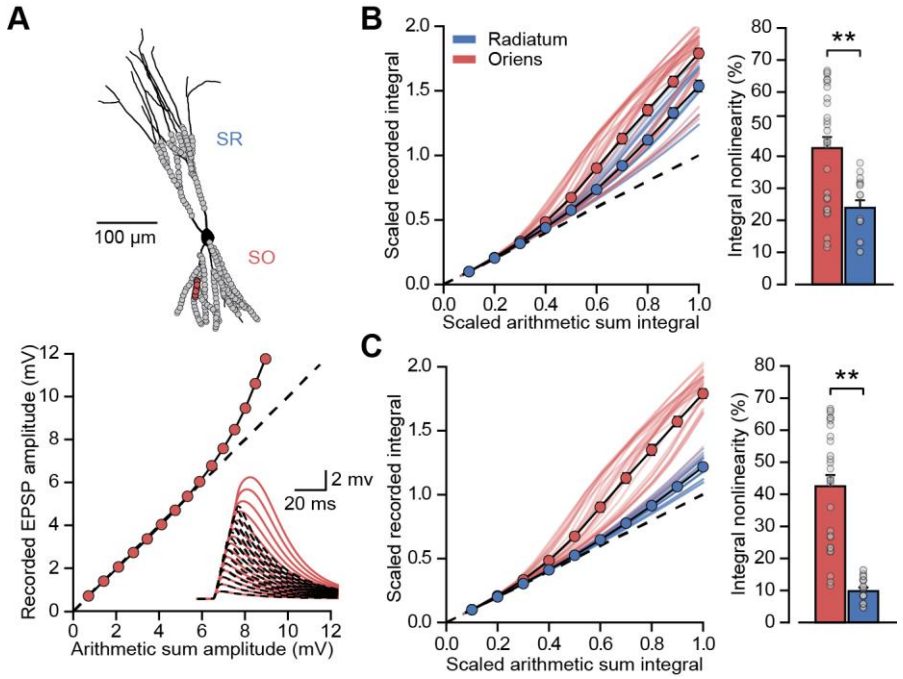

Figure 4. Differential NMDAR expression and dendrite morphology explain stratum-dependent synaptic integration difference.

(A) Reconstruction of a PV+ interneuron (axon not shown). Simulated synaptic locations are shown in gray. Bottom: example simulated uncaging experiment at the synapses marked with red circles; graph shows recorded EPSP amplitudes vs arithmetic sum of EPSP amplitudes. Inset: red solid lines, recorded summation; dashed black lines, arithmetic summation; waveforms calculated from individual synaptic responses.

(B) Scaled recorded time-integrals vs scaled arithmetic sum of time-integrals at all locations with equal NMDAR conductance (oriens locations: n=28, radiatum locations: n=16). Right: quantified synaptic integration nonlinearity.

(C) As (B), but with reduced NMDAR:AMPAR conductance ratio at radiatum dendrites.

NMDAR recruitment at feedback connections onto PV+ interneurons strengthens and stabilises neuronal assemblies.

In principal neurons, NMDAR-dependent supralinear dendritic integration increases their computational capacity (Mel, 1992). In its extreme case cooperativity among synapses could implement an AND gate where a somatic depolarization is conditional on more than one near-simultaneous excitatory input impinging on a dendritic branch.

bioRxiv preprint doi: https://doi.org/10.1101/279505; this version posted November 15, 2018. The copyright holder for this preprint (which was not certified by peer review) is the author/funder. All rights reserved. No reuse allowed without permission.

We asked how supralinear summation of feedback excitation of PV+ interneurons could affect local circuit behaviour. Feedback recruitment of interneurons has been implicated in lateral inhibition-like winner-takes-all mechanisms (de Almeida et al., 2009). We therefore simulated a network of spiking excitatory point neurons (Izhikevich, 2003) reciprocally connected to a single fast-spiking inhibitory neuron (Ferguson et al., 2013b, 2014) (**Figures 5A and 5B**). The inhibitory neuron received dual-component (AMPAR and NMDAR) synaptic conductances from the excitatory neurons (**Figure 5C**), and synapses located close to one another were allowed to interact cooperatively and engage the non-ohmic behaviour of NMDARs. The strength of interaction between individual excitatory synapses on the interneuron fell off with distance in an abstract input space (Figure S8), inspired by the experimental evidence for clustering of homotopic inputs on dendritic segments in principal neurons (Iacaruso et al., 2017; Wilson et al., 2016). Excitatory neurons were assumed to be driven by a Poisson process whose rate across the population was defined to be either clustered or dispersed in the input space. The overall intensity was such that the network entered a sparsely firing oscillatory state akin to a cortical gamma rhythm, with the simulated PV+ interneuron firing at around 40 Hz. Excitatory neurons driven by a compact 'hump' of excitation in input space cooperated in recruiting NMDARs on the interneuron to a greater extent than equivalent excitation shuffled randomly in input space (**Figure 5D**). The disproportionate NMDAR activation by compact versus distributed excitation recapitulates multiple co-active synapses within a small region of the dendritic tree cooperating to relieve NMDARs from Mg^{2+} blockade. Although individual pyramidal neurons fired sparsely, an effect of the gamma oscillation was to synchronize them so that the local depolarization was maximized.

Recruitment of NMDAR conductances in the interneuron also maintained sparse principal cell firing over several oscillatory cycles (Figure S9). In contrast, without NMDARs, the hump of active principal cells broadened as the oscillation stabilized. Principal cells at the core of the hump of activity (as defined by synaptic location on the interneuron dendritic tree) thus influence the firing of the interneuron disproportionately as a result of the recruitment of NMDARs. We propose, therefore, that NMDARs on PV+ interneurons contribute to maintaining a sharp assembly representation, dependent on the spatial arrangement of active synapses on the dendritic tree of the interneuron.

bioRxiv preprint doi: https://doi.org/10.1101/279505; this version posted November 15, 2018. The copyright holder for this preprint (which was not certified by peer review) is the author/funder. All rights reserved. No reuse allowed without permission.

Next, we simulated two similar networks mutually inhibiting one another (Geisler et al., 2007; Trouche et al., 2016) to understand how NMDARs in the inhibitory neurons could affect competition among cell assemblies. When one network received a stable and compact hump of excitation (again, with input space defined by location on the interneuron dendritic tree) it was much more likely to 'win' than a competing network receiving an equal amount of excitation that was dispersed (**Figure 6A**). This effect results from the additional interneuron depolarization mediated by NMDARs which were recruited by clustered synapses. The tendency for the network receiving a hump of excitation to win disappeared when NMDARs were removed from the inhibitory neurons (**Figures 6B and 6C**).

Finally, we explored the ability of the combined network to 'lock' onto one of two inputs of similar strength and compactness presented to the two sub-networks (**Figure 7**). An ethologically relevant analogous task in humans is the ability to stabilize perception of a Necker cube (**Figure 7A**). Although we make no claim as to how this task is solved, it exemplifies a situation where two sensory or cognitive representations compete for recruitment of a network. The net excitatory drive to each of the sub-networks was allowed to fluctuate independently with time **(Figure 7B)**. As a result of this stochastic variability in the input strength, and neuronal accommodation, the combined network intermittently 'flipped' between the two inputs. However, the frequency of flipping increased steeply when the normalized conductance of NMDARs was decreased in the inhibitory neurons, resulting in a flickering of the dominant assemblies (**Figure 7C**). In contrast, the frequency of flipping was relatively unaffected by reducing the AMPAR conductance (**Figure 7D**). We thus conclude that NMDAR-mediated cooperative interactions among clustered synapses on an interneuron stabilize cell assemblies.

bioRxiv preprint doi: https://doi.org/10.1101/279505; this version posted November 15, 2018. The copyright holder for this preprint (which was not certified by peer review) is the author/funder. All rights reserved. No reuse allowed without permission.

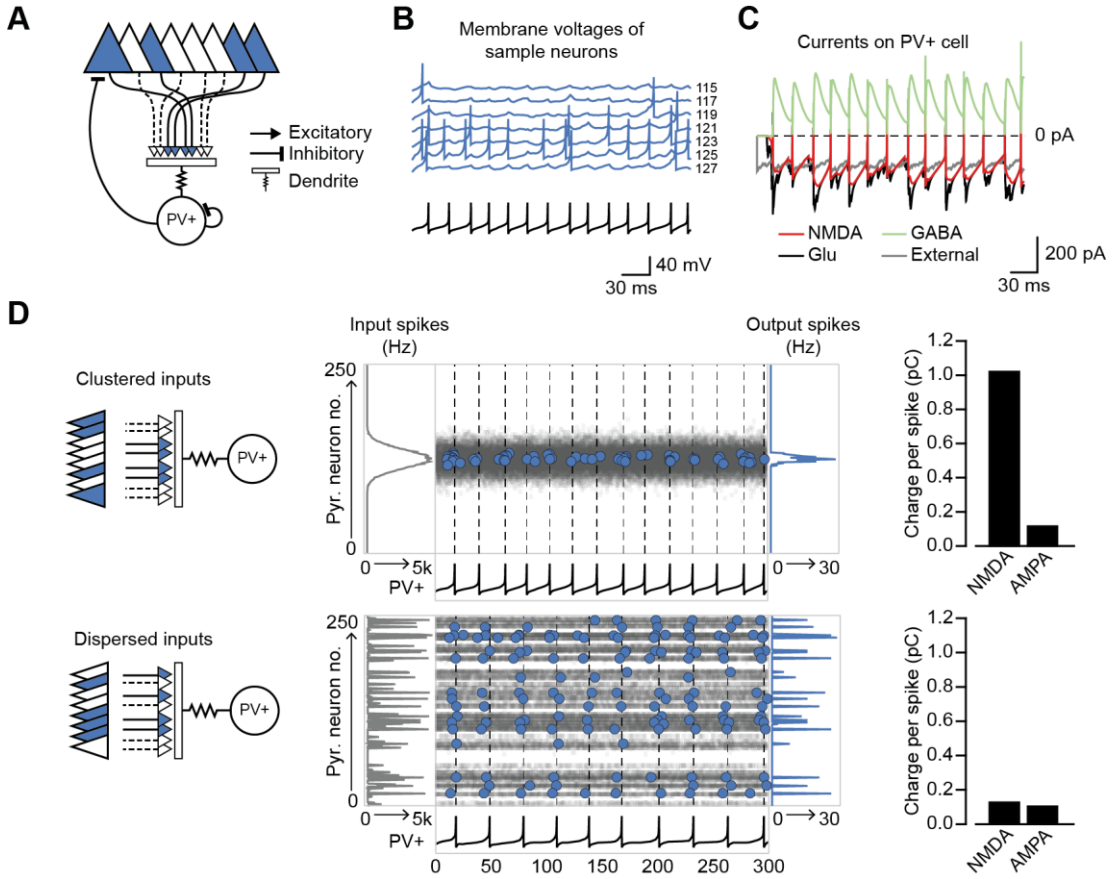

Figure 5. Network architecture and NMDAR recruitment at feedback connections.

(A) Schematic of network structure.

(B) Voltage traces of interneuron (black) and principal cells (blue, cell # at right) during network simulation. The network was driven by an asynchronous barrage of spikes, maximal in cell #125 ('clustered' input).

(C) Corresponding currents in interneuron.

(D) Left: schematic showing cell assemblies receiving clustered (top) or dispersed (bottom) external inputs, and middle: corresponding summary plots of network simulation showing external input distribution (grey), pyramidal cell firing (blue, circles), and interneuron firing (black, and vertical dashed lines). Right: average NMDAR and AMPAR charge in interneuron per principal neuron spike.

bioRxiv preprint doi: https://doi.org/10.1101/279505; this version posted November 15, 2018. The copyright holder for this preprint (which was not certified by peer review) is the author/funder. All rights reserved. No reuse allowed without permission.

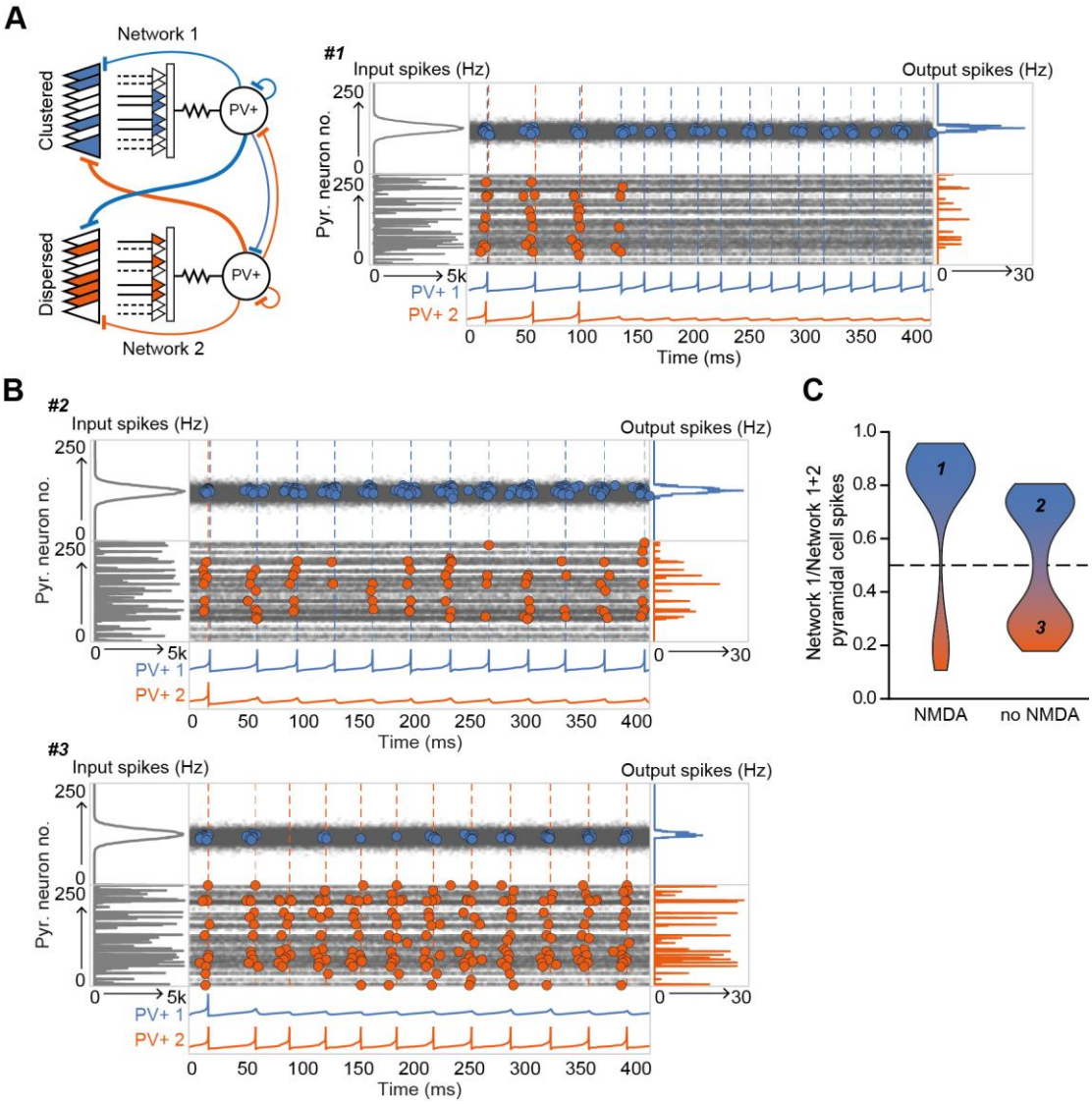

Figure 6. The role of NMDARs at feedback connections in cell assembly competition.

(A) Left: schematic showing competing cell assemblies with clustered (blue) or dispersed (orange) inputs; right: example simulation of lateral inhibition between these subnetworks with NMDARs at feedback connections to interneuron (input distribution: grey; pyramidal cell firing: blue/orange, circles; interneuron firing: blue/orange spikes and vertical dashed lines). The network receiving the clustered input out-competed the network receiving the dispersed input.

(B) Same as (A) but without NMDARs at feedback connections, showing, in one case (top), the clustered input winning, and in the other case (bottom), the dispersed input winning.

bioRxiv preprint doi: https://doi.org/10.1101/279505; this version posted November 15, 2018. The copyright holder for this preprint (which was not certified by peer review) is the author/funder. All rights reserved. No reuse allowed without permission.

(C) Summary of 250 simulations showing ratio of principal cell spikes for each subnetwork with and without NMDARs at feedback inputs onto interneuron. Numbers correspond to simulations illustrated in (A) and (B).

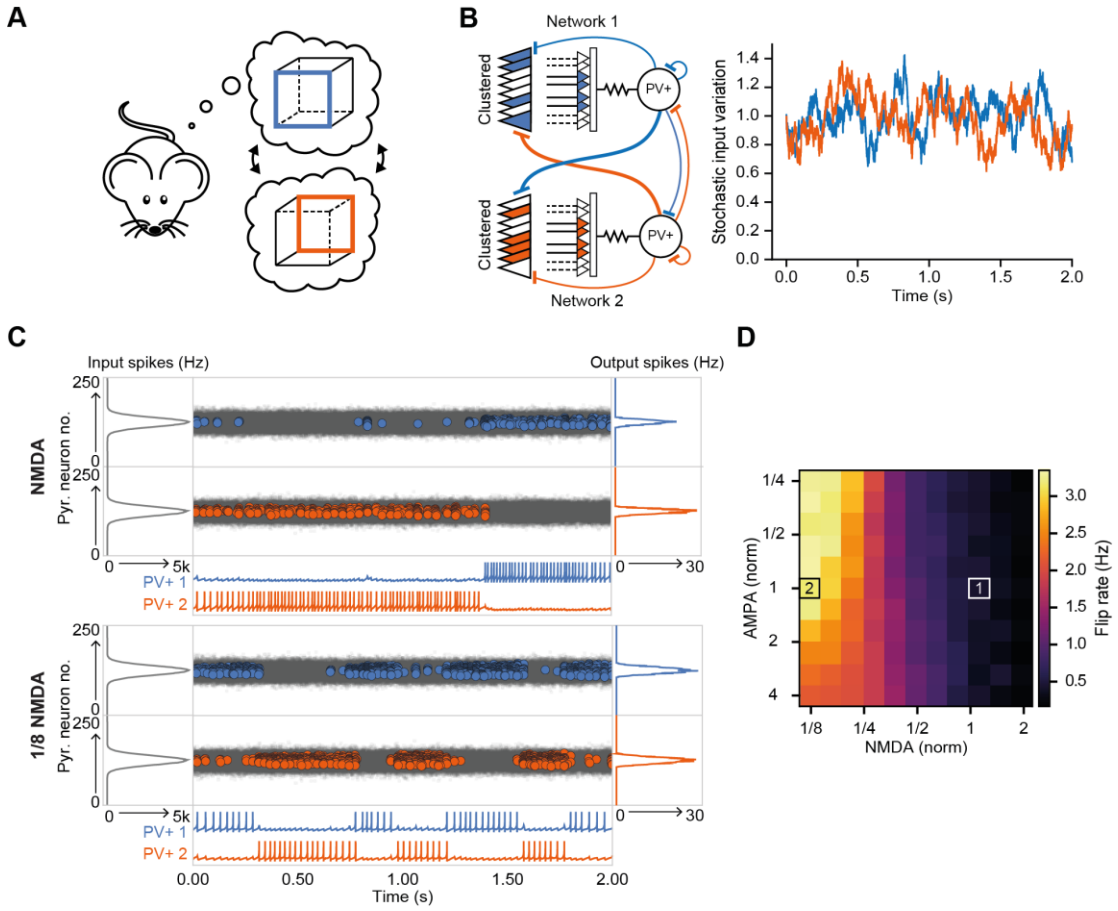

Figure 7. The role of NMDARs at feedback connections in cell assembly stability.

(A) Cartoon illustrating a bistable neural representation.

(B) Schematic of competing subnetworks both receiving clustered inputs (left) with random fluctuations in external input strength (plotted right).

(C) Example simulation of network activity with NMDARs at synapses on interneurons (top), and with NMDARs scaled down to 1/8 of baseline (bottom). Input distribution: grey; pyramidal cell firing: blue/orange, circles; interneuron firing: blue/orange spikes. Although the dominant networks flipped spontaneously in both cases, the frequency of flipping was much higher with the down-scaled NMDARs.

(D) Plot of network flip rate vs NMDAR and AMPAR conductance. White box labelled 1: baseline NMDAR simulation parameters; black box labelled 2: NMDARs down-scaled to 12.5%.

bioRxiv preprint doi: https://doi.org/10.1101/279505; this version posted November 15, 2018. The copyright holder for this preprint (which was not certified by peer review) is the author/funder. All rights reserved. No reuse allowed without permission.

Discussion

The present study shows that clustered excitatory synapses on stratum oriens dendrites of CA1 PV+ interneurons interact supralinearly. The high impedance of stratum oriens dendrites, which are innervated by axon collaterals of local pyramidal neurons, facilitates the cooperative recruitment of NMDARs. We place these results in the context of cell assembly competition by including nonlinear feedback integration in a spiking neural network model. NMDARs at synapses on a simulated feedback interneuron allow multiple principal cells co-innervating a subset of its input space, equivalent to a dendritic branch, to interact cooperatively in recruiting the interneuron. As a result, we found that cooperative assemblies are more able to efficiently engage interneurons in the inhibition of rival competing assembly representations. Furthermore, we report that inclusion of NMDAR conductances at feedback synapses stabilises cell assemblies, allowing the network to 'lock' on to an input. An adaptive role of NMDARs in feedback excitation of PV+ interneurons can therefore be to facilitate the emergence of strong and stable cell assemblies.

Extrapolating from the behaviour of a spiking neural network model to information processing clearly depends on a number of assumptions, not least that the principles underlying NMDAR-dependent input integration observed in CA1 PV+ interneurons apply generally throughout the brain, and that clustering of homotopic inputs on inhibitory dendritic segments obeys the same rules as in excitatory neurons (Iacaruso et al., 2017; Wilson et al., 2016). In addition, while PV+ cells predominantly show NMDAR-independent anti-Hebbian long-term potentiation (LTP) (Lamsa *et al.*, 2007), dependent on calcium-permeable AMPARs, feedback synapses also display NMDAR-dependent Hebbian plasticity rules (Le Roux et al., 2013). In this study we isolate the integrative properties of NMDARs from their role in synaptic plasticity, but it is expected that plasticity mechanisms may also contribute to the network phenomena described here. For example, NMDAR-dependent plasticity, which could be induced by cooperative feedback synaptic integration, would allow PV+ interneurons to be wired into stimulus-specific ensembles (Khan et al., 2018). Overall, therefore, NMDAR-dependent supralinear integration in the feedback inhibitory loop potentially expands the computational power of a canonical cortical motif.

bioRxiv preprint doi: https://doi.org/10.1101/279505; this version posted November 15, 2018. The copyright holder for this preprint (which was not certified by peer review) is the author/funder. All rights reserved. No reuse allowed without permission.

Selective knockdown of NMDARs in PV+ interneurons has previously been shown to cause a range of functional impairments, including working-memory deficits and a reduction in the precision of hippocampal spatial representations (Korotkova et al., 2010). The network simulations presented here provide a mechanistic explanation for some of these results, in particular, a reduction in spatial information conveyed by principal cell spiking (Korotkova et al., 2010). Other studies highlight a role for PV+ cells and inhibition in cell-assembly competition: in the visual cortex PV+ inhibition increases assembly similarity (Agetsuma et al., 2018), and in the hippocampus silencing of a dominant assembly was shown to uncover an alternative previously inhibited assembly (Trouche et al., 2016). The present study indicates that NMDARs may be integral to these functions.

Our network simulation results also resonate with multiple convergent findings that implicate PV+ cell NMDAR hypofunction at the centre of schizophrenia pathophysiology (Bygrave et al., 2016; Lisman et al., 2008; Nakazawa et al., 2012). For instance, NMDAR blockers have been shown to recapitulate some features of schizophrenia in healthy individuals (Krystal et al., 1994). When coupled with the observation that NMDAR antagonists cause a net disinhibition of principal cell activity (Homayoun and Moghaddam, 2007; Jackson et al., 2004), it has been suggested that cortical circuits are especially vulnerable to failure of NMDAR-mediated signalling in PV+ interneurons. Moreover, post-mortem studies have revealed a selective loss of PV+ interneurons in people with schizophrenia (Lewis et al., 2012) and overexpression of Neuregulin 1, a leading schizophrenia susceptibility gene, is associated with a reduction of NMDARs on PV+ cells (Kotzadimitriou et al., 2018) . Destabilisation of dominant neuronal assemblies, as shown here to result from impaired NMDAR signalling on PV+ interneurons, may thus explain a failure of sensory gating (Javitt and Freedman, 2015) and evidence for reduced cognitive control, for instance in the Necker cube test (McBain et al., 2011), in schizophrenia.

Feedback inhibition, such as that mediated by PV+ interneurons, is thought to be critical for preventing runaway excitation. Indeed, a failure of feedback inhibitory restraint is a major factor in the emergence of pathological states such as epileptic seizures. Given the importance of inhibition, how then do PV+ interneurons participate in assemblies that are composed of cells that they also regulate? One

bioRxiv preprint doi: https://doi.org/10.1101/279505; this version posted November 15, 2018. The copyright holder for this preprint (which was not certified by peer review) is the author/funder. All rights reserved. No reuse allowed without permission.

possibility is that PV+ cells are "transient allies" (Buzsáki, 2010), only aligning with principal cell assemblies over short time windows and at specific times. For example, in a recent study of circuit changes in the visual cortex during learning, PV+ cells were found to became more selective to task-relevant stimuli by increasing their coupling to stimuli selective principal cells and becoming less influenced by the general activity of the remaining surrounding network (Khan et al., 2018).

It is worth noting that feedback interneurons operating over longer time scales, for example somatostatin-positive oriens-lacunosum/moleculare interneurons, or cholecystokinin-expressing basket cells, may also be suited to mediate assembly competition. However, once recruited they would disengage more slowly because they integrate principal cell firing over a longer time frame. In contrast, PV+ cell firing is thought to define the period for gamma oscillations. As a result, NMDARs on PV+ interneurons are ideally suited to allow for stable assemblies while the stimulus is constant, but also allow for quick switching if the nature of the stimulus changes.

Recurrent connections between PV+ interneurons and local pyramidal cell circuits are found throughout the brain. A challenge for future studies will be to establish whether feedback connections outside of hippocampal area CA1 also display NMDAR-dependent supralinear feedback integration. Furthermore, experiments acutely and specifically blocking NMDARs at feedback synapses onto PV+ cells, as opposed to nonspecific knockdown of all PV+ cell NMDARs during development, will be necessary in order to fully characterize the importance of PV+ cell NMDAR processing *in vivo*. Taken together, our results expand the computational role of NMDARs on PV+ cells, providing a parsimonious mechanism uniting a number of hitherto unexplained observations, relating to both basic neuronal network function and pathophysiology.

Acknowledgements:
We are grateful to members of the Experimental Epilepsy Group at the UCL Institute of Neurology, Peter Latham and Arnd Roth for advice and technical assistance. This work was supported by the Wellcome Trust and the Brain Research Trust.

bioRxiv preprint doi: https://doi.org/10.1101/279505; this version posted November 15, 2018. The copyright holder for this preprint (which was not certified by peer review) is the author/funder. All rights reserved. No reuse allowed without permission.

References

Agetsuma, M., Hamm, J.P., Tao, K., Fujisawa, S., and Yuste, R. (2018). Parvalbumin-Positive Interneurons Regulate Neuronal Ensembles in Visual Cortex. Cereb. Cortex *28*, 1831–1845.

de Almeida, L., Idiart, M., and Lisman, J.E. (2009). A second function of gamma frequency oscillations: an E%-max winner-take-all mechanism selects which cells fire. J. Neurosci. Off. J. Soc. Neurosci. *29*, 7497–7503.

Amaral, D.G., Dolorfo, C., and Alvarez-Royo, P. (1991). Organization of CA1 projections to the subiculum: A PHA-L analysis in the rat. Hippocampus *1*, 415–435.

Bowie, D., Lange, G.D., and Mayer, M.L. (1998). Activity-dependent modulation of glutamate receptors by polyamines. J. Neurosci. at <http://eutils.ncbi.nlm.nih.gov/entrez/eutils/elink.fcgi?dbfrom=pubmed&id=97634 64&retmode=ref&cmd=prlinks>

Branco, T., Clark, B.A., and Häusser, M. (2010). Dendritic discrimination of temporal input sequences in cortical neurons. Science. *329*, 1671–1675.

Buzsáki, G. (2010). Neural Syntax: Cell Assemblies, Synapsembles, and Readers. Neuron *68*, 362–385.

Bygrave, A.M., Masiulis, S., Nicholson, E., Berkemann, M., Barkus, C., Sprengel, R., Harrison, P.J., Kullmann, D.M., Bannerman, D.M., and Kätzel, D. (2016). Knockout of NMDA-receptors from parvalbumin interneurons sensitizes to schizophrenia-related deficits induced by MK-801. Transl. Psychiatry *6*, e778.

Carlén, M., Meletis, K., Siegle, J.H., Cardin, J.A., Futai, K., Vierling-Claassen, D., Rühlmann, C., Jones, S.R., Deisseroth, K., Sheng, M., et al. (2012). A critical role for NMDA receptors in parvalbumin interneurons for gamma rhythm induction and behavior. Mol. Psychiatry *17*, 537–548.

Carnevale, N.T., and Hines, M.L. (2009). The NEURON Book (Cambridge University Press).

Chiovini, B., Turi, G., Katona, G., Kaszás, A., Pálfi, D., Maák, P., Szalay, G., Szabó,

bioRxiv preprint doi: https://doi.org/10.1101/279505; this version posted November 15, 2018. The copyright holder for this preprint (which was not certified by peer review) is the author/funder. All rights reserved. No reuse allowed without permission.

M., Szabó, G., Szadai, Z., et al. (2014). Dendritic Spikes Induce Ripples in Parvalbumin Interneurons during Hippocampal Sharp Waves. Neuron *82*, 908–924.

Coyle, J.T. (2012). NMDA receptor and schizophrenia: A brief history. Schizophr. Bull. *38*, 920–926.

Cuntz, H., Forstner, F., Borst, A., and Häusser, M. (2010). One rule to grow them all: a general theory of neuronal branching and its practical application. PLoS Comput. Biol. *6*.

delPino, I., García-Frigola, C., Dehorter, N., Brotons-Mas, J.R., Alvarez-Salvado, E., MartínezdeLagrán, M., Ciceri, G., Gabaldón, M.V., Moratal, D., Dierssen, M., et al. (2013). Erbb4 Deletion from Fast-Spiking Interneurons Causes Schizophrenia-like Phenotypes. Neuron *79*, 1152–1168.

Deuchars, J., and Thomson, A.M. (1996). CA1 pyramid-pyramid connections in rat hippocampus in vitro: Dual intracellular recordings with biocytin filling. Neuroscience *74*, 1009–1018.

Ferguson, K. a, Huh, C.Y.L., Amilhon, B., Williams, S., and Skinner, F.K. (2013a). Experimentally constrained CA1 fast-firing parvalbumin-positive interneuron network models exhibit sharp transitions into coherent high frequency rhythms. Front. Comput. Neurosci. *7*, 144.

Ferguson, K.A., Huh, C.Y.L., Amilhon, B., Williams, S., and Skinner, F.K. (2013b). Experimentally constrained CA1 fast-firing parvalbumin-positive interneuron network models exhibit sharp transitions into coherent high frequency rhythms. Front. Comput. Neurosci. *7*, 144.

Ferguson, K.A., Huh, C.Y.L., Amilhon, B., Williams, S., and Skinner, F.K. (2014). Simple, biologically-constrained CA1 pyramidal cell models using an intact, whole hippocampus context. F1000Research *3*, 104.

Gasparini, S. (2006). State-Dependent Dendritic Computation in Hippocampal CA1 Pyramidal Neurons. J. Neurosci. *26*, 2088–2100.

Geisler, C., Robbe, D., Zugaro, M., Sirota, A., and Buzsáki, G. (2007). Hippocampal

bioRxiv preprint doi: https://doi.org/10.1101/279505; this version posted November 15, 2018. The copyright holder for this preprint (which was not certified by peer review) is the author/funder. All rights reserved. No reuse allowed without permission.

place cell assemblies are speed-controlled oscillators. Proc. Natl. Acad. Sci. *104*, 8149–8154.

Gulyás, A.I., Megías, M., Emri, Z., and Freund, T.F. (1999). Total number and ratio of excitatory and inhibitory synapses converging onto single interneurons of different types in the CA1 area of the rat hippocampus. J. Neurosci. *19*, 10082–10097.

Hines, M.L., and Carnevale, N.T. (1997). The NEURON simulation environment. Neural Comput. *9*, 1179–1209.

Homayoun, H., and Moghaddam, B. (2007). NMDA Receptor Hypofunction Produces Opposite Effects on Prefrontal Cortex Interneurons and Pyramidal Neurons. J. Neurosci. *27*, 11496–11500.

Hu, H., and Jonas, P. (2014). A supercritical density of Na(+) channels ensures fast signaling in GABAergic interneuron axons. Nat. Neurosci. *17*, 686–693.

Hu, H., Martina, M., and Jonas, P. (2010). Dendritic mechanisms underlying rapid synaptic activation of fast-spiking hippocampal interneurons. Science *327*, 52–58.

Iacaruso, M.F., Gasler, I.T., and Hofer, S.B. (2017). Synaptic organization of visual space in primary visual cortex. Nature *547*, 449–452.

Izhikevich, E.M. (2003). Simple model of spiking neurons. IEEE Trans. Neural Networks *14*, 1569–1572.

Jackson, M.E., Homayoun, H., and Moghaddam, B. (2004). NMDA receptor hypofunction produces concomitant firing rate potentiation and burst activity reduction in the prefrontal cortex. Proc. Natl. Acad. Sci. *101*, 8467–8472.

Javitt, D.C., and Freedman, R. (2015). Sensory processing dysfunction in the personal experience and neuronal machinery of schizophrenia. Am. J. Psychiatry *172*, 17–31.

Jonas, P., Bischofberger, J., Fricker, D., and Miles, R. (2004). Interneuron Diversity series: Fast in, fast out – temporal and spatial signal processing in hippocampal interneurons. Trends Neurosci. *27*, 30–40.

Kerlin, A.M., Andermann, M.L., Berezovskii, V.K., and Reid, R.C. (2010). Broadly

bioRxiv preprint doi: https://doi.org/10.1101/279505; this version posted November 15, 2018. The copyright holder for this preprint (which was not certified by peer review) is the author/funder. All rights reserved. No reuse allowed without permission.

Tuned Response Properties of Diverse Inhibitory Neuron Subtypes in Mouse Visual Cortex. Neuron *67*, 858–871.

Khan, A.G., Poort, J., Chadwick, A., Blot, A., Sahani, M., Mrsic-flogel, T.D., and Hofer, S.B. (2018). selectivity and interactions of GABAergic interneuron classes in visual cortex. Nat. Neurosci. *21*.

Korotkova, T., Fuchs, E.C., Ponomarenko, A., von Engelhardt, J., and Monyer, H. (2010). NMDA Receptor Ablation on Parvalbumin-Positive Interneurons Impairs Hippocampal Synchrony, Spatial Representations, and Working Memory. Neuron *68*, 557–569.

Kotzadimitriou, D., Nissen, W., Paizs, M., Newton, K., Harrison, P.J., Paulsen, O., and Lamsa, K. (2018). Neuregulin 1 Type-I over-Expression Is Associated with Reduced NMDA Receptor-Mediated Synaptic Signaling in Hippocampal Interneurons Expressing PV or CCK. ENeuro *5*.

Krystal, J., Karper, L., Seibyl, J., Freeman, G., Delaney, R., Bremner, D., Heninger, G., Bowers, M., and Charney, D. (1994). Subanesthetic effects of the NMDA antagonist, ketamine, in humans: psychotomimetic, perceptual, cognitive, and neuroendocrine effects. Arch Gen Psychiatry *51*, 199–214.

Lamsa, K.P., Heeroma, J.H., Somogyi, P., Rusakov, D.A., and Kullmann, D.M. (2007a). Anti-hebbian long-term potentiation in the hippocampal feedback inhibitory circuit. Science *315*, 1262–1266.

Lamsa, K.P., Heeroma, J.H., Somogyi, P., Rusakov, D.A., and Kullmann, D.M. (2007b). Anti-Hebbian Long-Term Potentiation in the Hippocampal Feedback Inhibitory Circuit. Science *315*, 1262–1266.

Lewis, D.A., Curley, A.A., Glausier, J.R., and Volk, D.W. (2012). Cortical parvalbumin interneurons and cognitive dysfunction in schizophrenia. Trends Neurosci. *35*, 57–67.

Lisman, J.E., Coyle, J.T., Green, R.W., Javitt, D.C., Benes, F.M., Heckers, S., and Grace, A.A. (2008). Circuit-based framework for understanding neurotransmitter and risk gene interactions in schizophrenia. Trends Neurosci. *31*, 234–242.

bioRxiv preprint doi: https://doi.org/10.1101/279505; this version posted November 15, 2018. The copyright holder for this preprint (which was not certified by peer review) is the author/funder. All rights reserved. No reuse allowed without permission.

Losonczy, A., and Magee, J.C. (2006). Integrative properties of radial oblique dendrites in hippocampal CA1 pyramidal neurons. Neuron *50*, 291–307.

Matta, J.A., Pelkey, K.A., Craig, M.T., Chittajallu, R., Jeffries, B.W., and McBain, C.J. (2013). Developmental origin dictates interneuron AMPA and NMDA receptor subunit composition and plasticity. Nat. Neurosci. *16*, 1032–1041.

McBain, R., Norton, D.J., Kim, J., and Chen, Y. (2011). Reduced cognitive control of a visually bistable image in schizophrenia. J. Int. Neuropsychol. Soc. *17*, 551–556.

Mel, B.W. (1992). NMDA-Based Pattern Discrimination in a Modeled Cortical Neuron. Neural Comput. *4*, 502–517.

Nakazawa, K., Zsiros, V., Jiang, Z., Nakao, K., Kolata, S., Zhang, S., and Belforte, J.E. (2012). GABAergic interneuron origin of schizophrenia pathophysiology. Neuropharmacology *62*, 1574–1583.

Nörenberg, A., Hu, H., Vida, I., Bartos, M., and Jonas, P. (2010). Distinct nonuniform cable properties optimize rapid and efficient activation of fast-spiking GABAergic interneurons. Proc. Natl. Acad. Sci. U. S. A. *107*, 894–899.

Poirazi, P., and Mel, B.W. (2001). Impact of active dendrites and structural plasticity on the memory capacity of neural tissue. Neuron *29*, 779–796.

Pouille, F., and Scanziani, M. (2001). Enforcement of temporal fidelity in pyramidal cells by somatic feed-forward inhibition. Science *293*, 1159–1163.

Pouille, F., and Scanziani, M. (2004). Routing of spike series by dynamic circuits in the hippocampus. Nature *429*, 717–723.

Pouille, F., Marin-Burgin, A., Adesnik, H., Atallah, B. V, and Scanziani, M. (2009). Input normalization by global feedforward inhibition expands cortical dynamic range. Nat. Neurosci. *12*, 1577–1585.

Roth, A., and van Rossum, M.C.W. (2009). Modeling Synapses. Comput. Model. Methods Neurosci. *06*, 139–160.

Le Roux, N., Cabezas, C., Böhm, U.L., and Poncer, J.C. (2013). Input-specific

bioRxiv preprint doi: https://doi.org/10.1101/279505; this version posted November 15, 2018. The copyright holder for this preprint (which was not certified by peer review) is the author/funder. All rights reserved. No reuse allowed without permission.

learning rules at excitatory synapses onto hippocampal parvalbumin-expressing interneurons. J. Physiol. *591*, 1809–1822.

Stuart, G.J., and Spruston, N. (2015). Dendritic integration: 60 years of progress. Nat. Neurosci. *18*, 1713–1721.

Trouche, S., Perestenko, P. V, van de Ven, G.M., Bratley, C.T., McNamara, C.G., Campo-Urriza, N., Black, S.L., Reijmers, L.G., and Dupret, D. (2016). Recoding a cocaine-place memory engram to a neutral engram in the hippocampus. Nat. Neurosci. *19*, 564–567.

Wang, X.J., and Buzsáki, G. (1996). Gamma oscillation by synaptic inhibition in a hippocampal interneuronal network model. J. Neurosci. *16*, 6402–6413.

Williams, S.R., and Mitchell, S.J. (2008). Direct measurement of somatic voltage clamp errors in central neurons. Nat. Neurosci. *11*, 790–798.

Wilson, D.E., Whitney, D.E., Scholl, B., and Fitzpatrick, D. (2016). Orientation selectivity and the functional clustering of synaptic inputs in primary visual cortex. Nat. Neurosci. *19*, 1003–1009.

bioRxiv preprint doi: https://doi.org/10.1101/279505; this version posted November 15, 2018. The copyright holder for this preprint (which was not certified by peer review) is the author/funder. All rights reserved. No reuse allowed without permission.

Materials and Methods

Animals

Hippocampal slices were obtained from postnatal day 14 – 24 male and female mice, or from 2-3 month old male and female mice (optogenetic experiments), expressing tdTomato in PV+ interneurons. Experimental mice were obtained by crossing homozygous mice expressing Cre under the PV promoter (Jackson Labs: B6;129P2-Pvalb$^{tm1(cre)Arbr}$) with homozygous Ai9 Cre reporter mice (Jackson Labs: B6.Cg-*Gt(ROSA)26Sor*$^{tm9(CAG\text{-}tdTomato)Hze}$). Animals were group-housed under a non-reversed 12 h light/dark cycle, and allowed access to food and water *ad libitum*. All procedures were carried out in accordance with the UK Animals (Scientific Procedures) Act, 1986.

Surgery for viral injections

Mice (minimum age: 6 weeks) were anaesthetized with isoflurane and viruses were stereotaxically injected into the dorsal CA1 region of both hippocampi using a Hamilton syringe. The injection coordinates were 2.15 mm caudal and 1.4 mm lateral of Bregma, and 1.2 and 1.0 mm deep from the pia. 50 nl of virus was injected at each site at a rate of 100 nl/min, and the needle was left in place for 5 minutes following injections before withdrawal. Slices were prepared for experiments after a minimum of three weeks post-surgery.

Slice preparation and electrophysiology

Acute sagittal brain slices (300 µm) were prepared using a Vibratome (Leica VT1200 S). Slices were cut in an ice-cold artificial cerebrospinal fluid (ACSF) solution, containing (in mM): NaCl (119), KCl (2.5), NaH_2PO_4 (1.25), $NaHCO_3$ (25), glucose (20), $CaCl_2$ (1.5), $MgSO_4$ (1.3), and saturated with 95% O_2, 5% CO_2. Slices were allowed to recover at 32˚C for 15 min after slicing, before subsequent storage in ACSF at room temperature. Older mice (>1 month) were transcardially perfused with ice-cold sucrose-based ACSF solution, containing (in mM): sucrose (75), NaCl (87), KCl (2.5), NaH_2PO_4 (1.25), $NaHCO_3$ (25), glucose (25), $CaCl_2$ (0.5), $MgCl_2$ (7), and saturated with 95% O_2, 5% CO_2. Slices were cut in the same solution, and left to recover at 32˚C for 15 min, before being

bioRxiv preprint doi: https://doi.org/10.1101/279505; this version posted November 15, 2018. The copyright holder for this preprint (which was not certified by peer review) is the author/funder. All rights reserved. No reuse allowed without permission.

transferred to normal ACSF (same as above but with 2.5 mM $CaCl_2$) for storage at room temperature. All experiments were carried out in ACSF maintained at 30° – 32°C and perfused at 2–3 ml/min. For dissection of AMPAR and NMDAR components at feedforward and feedback synapses (**Figures 1A and 1B**) a modified ACSF containing 0.1 mM $MgSO_4$ was used to partially relieve Mg^{2+} blockade of NMDARs at rest. NMDARs and AMPARs were sequentially blocked with D-AP5 (100 μM) and 2,3-dihydroxy-6-nitro-7-sulfamoyl-benzo[f]quinoxaline-2,3-dione (NBQX, 10 μM), respectively. Picrotoxin (100 μM) and CGP 55845 (1 μM) were included throughout these experiments, as well as the HCN channel blocker ZD 7288 (30 μM), which was included in order to hyperpolarize pyramidal cells and decrease network excitability. Picrotoxin (100 μM) and CGP 55845 (1 μM) were also included throughout the optogenetic experiments (**Figures 1C-1F**). For blockade of NMDARs or Na^+ channels during uncaging experiments (**Figure 3**) D-AP5 (100 μM) or TTX (0.1 μM) were used, respectively.

Fluorescence-guided somatic whole-cell recordings were obtained from PV+ interneurons and pyramidal cells using a Multiclamp 700B amplifier (Molecular Devices), filtered at 5 kHz, and digitized at 20 kHz (National Instruments PCI-6221), with custom software written in LabVIEW. Patch pipettes of 3 – 4 MΩ resistance were filled with a KGluconate-based internal solution, containing (in mM): KGluconate (140), KOH-HEPES (10), EGTA (0.2), NaCl (8), Mg-ATP (2), Na-GTP (0.3), Mg-ATP (5). Cells were held at -60 mV during voltage-clamp experiments (**Figure 1A and 1B**). All other experiments were performed in current-clamp mode, and current was continuously injected to maintain cell membrane between -65 and -70 mV. The series resistance during recordings was < 25 MΩ. For field stimulation experiments, concentric bipolar stimulating electrodes (FHC) coupled to constant current stimulators (Digitimer) were placed in the alveus and stratum radiatum in order to evoke responses from feedback and feedforward inputs, respectively (Pouille and Scanziani, 2004). Stimuli were delivered to each pathway at 0.05 Hz, and alternated between the pathways. Optogenetic responses were elicited using 470 nm light pulses (1 ms, 1-15 mW) at 0.2 Hz, generated by an LED light-source (ThorLabs) and delivered

bioRxiv preprint doi: https://doi.org/10.1101/279505; this version posted November 15, 2018. The copyright holder for this preprint (which was not certified by peer review) is the author/funder. All rights reserved. No reuse allowed without permission.

through a 40X objective lens (Olympus). The light power necessary to illicit maximal and minimal responses was identified for each cell, and the difference in power was divided by 5 to define the 5 stimulation strengths (20%, 40%, 60%, 80% and 100%) used in each cycle. Maximal responses were identified as the maximum response elicited without generating an action potential (typically ≤ 15 mV), and minimal responses were the smallest response visible.

Two-photon imaging and uncaging experiments

Slices were submerged in a perfusion chamber on an upright microscope (FV1000 BX61, Olympus). Simultaneous two-photon imaging and uncaging of MNI-caged glutamate was performed with two Ti-sapphire lasers tuned to 810 nm and 720 nm, for imaging and uncaging respectively (Mai-Tai, Spectra Physics; Chameleon, Coherent). MNI-caged-glutamate-TFA (3 mM; Femtonics) dissolved in the recording ACSF solution was perfused in a closed system.

Uncaging locations (between 8 and 12) were selected either side of a dendritic region of interest, separated by 2 – 3 μm and within 1 μm of the dendrite. Uncaging-evoked EPSPs (uEPSPs) were evoked using 0.5 ms-long pulses of 720 nm laser-light. To account for differing depths of dendritic segments, uncaging-laser intensity was adjusted using a Pockels Cell (Conoptics). uEPSPs were first evoked by sequential stimulation of individual uncaging spots with an inter-stimulus interval of 200 ms. Uncaging locations (order chosen at random) were then stimulated at intervals of 1 ms, with 10 s delays between trials. Beginning with a single location, the number of uncaging locations was increased on successive trials until all locations were activated. The entire sequence was repeated between 2 and 5 times, without changing the order of uncaging locations, and the responses to each combination of uncaging locations were averaged. Arithmetic compound uEPSPs were constructed from individual spot recordings offline, including a 1 ms waveform shift to match the experimental protocol, and compared to recorded uEPSPs. Uncaging times and locations were controlled by scanning software (Fluoview 1000V) and a pulse generator (Berkeley Nucleonics) coupled to the Pockels cell. Experiments were

bioRxiv preprint doi: https://doi.org/10.1101/279505; this version posted November 15, 2018. The copyright holder for this preprint (which was not certified by peer review) is the author/funder. All rights reserved. No reuse allowed without permission.

discontinued and excluded from analysis if photo-damage to PV+ cells was observed, or if physical drift occurred.

Quantification and statistical analysis

Data analysis was performed using custom code written in Python. The nonlinearity of responses recorded from uncaging at each dendritic location was quantified using the following equation:

$$nonlinearity\ \% = \sum_{i=2}^{n} \frac{\frac{Mi}{Ai} - 1}{n-1} \,.\, 100\% \qquad ((1)$$

where Mi is the amplitude of the ith measured uEPSP (composed of i individual uncaging spots), Ai is the amplitude of the ith constructed arithmetic summed uEPSP, and n is the total number of uncaging locations. For uEPSP integral analysis a Savitzky-Golay filter was applied to traces.

For analysis of NMDAR:AMPAR ratios, pharmacologically "isolated" NMDAR and AMPAR traces were extracted via subtraction of EPSC waveforms. To isolate the AMPAR component, EPSCs recorded in NBQX were subtracted from baseline EPSCs, and the NMDAR component calculated from subtraction of the EPSPCs in both NBQX and D-AP5 from those recorded in NBQX only. NMDAR and AMPAR charge were then calculated by integrating the first 500 ms or 20 ms, respectively, of these isolated traces (**Figure 3C**).

Statistical significance was assessed using Student's paired or unpaired *t*-tests. Data are presented as mean ± SEM, unless stated otherwise.

Multi-compartmental modelling

Multi-compartmental modelling was performed with the NEURON simulation environment (Hines and Carnevale, 1997). The soma and dendrites of a PV+ interneuron were reconstructed using the TREES toolbox in MATLAB (Cuntz et

bioRxiv preprint doi: https://doi.org/10.1101/279505; this version posted November 15, 2018. The copyright holder for this preprint (which was not certified by peer review) is the author/funder. All rights reserved. No reuse allowed without permission.

al., 2010). The axon was not included in the reconstruction. As PV+ interneuron dendrites are generally smooth, addition of spines or correction of synaptic responses for spines was deemed unnecessary. The number of segments per section was constrained to odd numbers and set according to the d-lambda rule (Carnevale and Hines, 2009) to have a length no more than 10% of the alternating current length constant at 1 kHz. The model contained 500 segments in total with a maximal segment length of 8.7 µm.

The biophysical parameters were based on previously published models of dentate gyrus PV+ basket cells (Hu and Jonas, 2014; Nörenberg et al., 2010). The specific membrane capacitance (C_m) and intracellular resistance (R_i) were assumed to be spatially uniform (for values see Table 2.1). In contrast, the specific membrane resistance (R_m) was assumed to vary as a step function with distance from the soma. R_m at distal dendrites was 10 times larger than at proximal dendrites, and R_m was chosen so as to make the model cell's input resistance 78 MΩ, the mean experimentally recorded input resistance (78.6 ± 5.2 MΩ). The border between proximal and distal dendrites was defined to be 120 µm from the soma.

Table 1: NEURON model parameters

Parameter	Proximal	Distal	Units
C_m	0.9	0.9	$\mu F\ cm^{-2}$
R_{axial}	170	170	$\Omega\ cm^{-1}$
R_m	5.55	55.5	$k\Omega\ cm^2$
e_{leak}	-65	-	mV
e_{gK}	-90	-	mV
e_{gNa}	55	-	mV
vshift	-12	-12	mV
g_k dend	300	300	$pS\ \mu m^{-2}$
g_{Na} dend	200	100	$pS\ \mu m^{-2}$
g_{Na} soma	2000	-	$pS\ \mu m^{-2}$

Wang and Buzsaki (WB) Na^+ and K^+ channels were inserted in the model neuron to confer a fast-spiking action potential phenotype (Wang and Buzsáki, 1996). However, in order to produce a realistic firing frequency - current injection relationship a hyperpolarizing voltage shift was included in the WB

bioRxiv preprint doi: https://doi.org/10.1101/279505; this version posted November 15, 2018. The copyright holder for this preprint (which was not certified by peer review) is the author/funder. All rights reserved. No reuse allowed without permission.

implementation. The depolarized threshold of the WB mechanism has been discussed previously (Ferguson et al., 2013a).

Subthreshold synaptic integration curves were produced by first finding all sites on the dendritic tree that were located between 40 and 190 µm from the soma. Simulations then closely followed the experimental protocol detailed above. At each dendritic site, 15 synapses were placed within a distance of 30 µm. Each synapse was activated individually and the arithmetic sum calculated from the somatic membrane potential. Synapses were then activated in increasing numbers, with an interval of 1 ms between activations, and the integral and amplitude of these measured responses compared to the calculated arithmetic responses. Quantification of dendritic nonlinearity was identical to that applied to experimental data.

Network modelling

Single cell modelling

For network simulations, PV+ interneurons and CA1 pyramidal cells were represented by two-dimensional Izhikevich model neurons (Izhikevich, 2003). Izhikevich models for these neurons have previously been parameterized from experimental data (Ferguson et al., 2013b, 2014). In line with this previous work, the models were slightly modified to reproduce the narrow PV+ interneuron spike width, and had the following form:

$$C_m \frac{dv}{dt} = k(v - v_r)(v - v_t) - u + I_{applied}$$

$$\frac{du}{dt} = a[b(v - v_r) - u] \qquad (2)$$

$$if\ v \geq v_{peak}\text{, set } v = c,\ u = u + d$$

$$\text{Where } k = k_{low} \text{ if } v \leq v_t;\ k = k_{high} \text{ if } v > v_t$$

The variable v represents the membrane potential, and u represents a slow "refractory" current, that, aside from subthreshold effects governed by b, is increased by d when the neuron fires, and decays at a rate determined by a. The parameter C_m represents the membrane capacitance; k is a scalar; v_r is the

bioRxiv preprint doi: https://doi.org/10.1101/279505; this version posted November 15, 2018. The copyright holder for this preprint (which was not certified by peer review) is the author/funder. All rights reserved. No reuse allowed without permission.

resting membrane potential; v_t is the instantaneous spiking threshold potential; v_{peak} is the peak action potential voltage; $I_{applied}$ is the applied current, comprised of the sum of all synaptic inputs to the cell; a is the recovery inverse time constant of the refractory current, u; b is the sensitivity of u to subthreshold voltage fluctuations; c is the voltage reset value; and d is the amount of current generated by the after-spike behaviour. The values for all parameters of the network simulations are presented in Table 2.2

Synaptic modelling

Synaptic connections between neurons were modelled as bi-exponential, conductance-based synapses (Roth and van Rossum, 2009), which can be written in the following differential form:

$$\begin{aligned} g^{chan}(v^{syn}) &= \frac{G^{chan}(v^{syn})}{\tau_1^{chan} - \tau_2^{chan}}(g_1^{chan} - g_2^{chan}) \\ \frac{dg_1^{chan}}{dt} &= \left(\delta^{chan}(t) - \frac{1}{\tau_1^{chan}} g_1^{chan}\right) \\ \frac{dg_2^{chan}}{dt} &= \left(\delta^{chan}(t) - \frac{1}{\tau_2^{chan}} g_2^{chan}\right) \\ G^{NMDA}(v^{syn}) &= \left(\frac{1}{2} tanh\left[\frac{v_i^{syn} + 50mV}{10mV}\right] + \frac{1}{2}\right) \\ G^{AMPA}(v^{syn}) &= G^{ext}(v^{syn}) = G^{GABA}(v^{syn}) = 1 \end{aligned} \quad (3)$$

Where g^{chan} is the total synaptic conductance of a given channel family (composed of a rise term g_1^{chan} and a decay term g_2^{chan}), $G^{chan}(v^{syn})$ is an eventual instantaneous voltage-gating term dependent on a local synaptic voltage v^{syn}(only relevant for NMDA channels; detailed in the next section), τ_1^{chan} is the rising exponential time constant, τ_2^{chan} is the decay exponential time constant, the variable t is time, and $\delta^{chan}(t)$ represents the input spike train of Dirac deltas.

NMDA receptor modelling

NMDARs, present at the feedback connections from principal cells onto the interneuron, and the cooperative relief of NMDAR Mg^{2+} block by co-active synaptic inputs, were modelled in an abstract manner. We assumed that all co-

bioRxiv preprint doi: https://doi.org/10.1101/279505; this version posted November 15, 2018. The copyright holder for this preprint (which was not certified by peer review) is the author/funder. All rights reserved. No reuse allowed without permission.

active inputs from the population of n_{pyr} principal cells had a degree of cooperation, or functional clustering (Wilson et al., 2016), which was weighted by a distance matrix, $D^{n_{pyr} \times n_{pyr}}$. D was defined as a Toeplitz matrix, with the i_{th} element of the row vector $D_{\frac{n_{pyr}}{2}}$ equal to:

$$D_{\frac{n_{pyr}}{2},i} = \frac{1}{\sqrt{2\pi\, {\sigma_D}^2}} e^{-\frac{(i-n_{pyr}/2)^2}{2\,{\sigma_D}^2}} \tag{4}$$

Where ${\sigma_D}^2$ controlled the specificity of local cooperation. We then modelled the time evolution of the voltage of the local synaptic membrane patch, v_i^{syn}, with the following equation:

$$C_{syn}\frac{dv_i^{syn}}{dt} = k^{syn} I_i^{syn} + g^{leak}\left(e^{leak} - v_i^{syn}\right) \tag{5}$$

$$I_i^{syn} = \sum_{j=1}^{n_{pyr}} D_{i,j}\left(k_{pv+}^{AMPA} g_j^{AMPA} + k_{pv+}^{NMDA} g_j^{NMDA}(v_j^{syn})\right)\left(e^{glu} - v_i^{syn}\right)$$

Where C_{syn} is the local patch membrane capacitance, k^{syn} is a gain applied to the input current I_i^{syn}, k_{pv+}^{chan} are gain constants defining each channel family synaptic strength onto the interneuron, g^{leak} is a leak conductance with reversal potential e^{leak}.

Finally, the total current, $I_{applied}$, an interneuron receives is given by:

$$I_{applied} = \left(\sum_{i=1}^{n_{pyr}} k_{pv+}^{AMPA}\, g_i^{AMPA} + k_{pv+}^{NMDA} g_i^{NMDA}\left(v_i^{syn}\right) + k_{pv+}^{ext}\, g_i^{ext}\right)(e^{glu} - v) + k_{pv+}^{GABA}\left(\sum_{i=1}^{n_{pv+}} g_i^{GABA}\right)(e^{GABA} - v) \tag{6}$$

Accordingly, for the *ith* pyramidal cell the input current is more simply given by:

$$I_{Applied}^{i} = k_{pyr}^{ext}\, g_i^{ext}(e^{glu} - v) + k_{pyr}^{GABA}\left(\sum_{i=1}^{n_{pv+}} g_i^{GABA}\right)(e^{GABA} - v) \tag{7}$$

External inputs

The external input to the i_{th} pyramidal neuron was modelled as a non-homogeneous Poisson process, in which the instantaneous rate of incoming

bioRxiv preprint doi: https://doi.org/10.1101/279505; this version posted November 15, 2018. The copyright holder for this preprint (which was not certified by peer review) is the author/funder. All rights reserved. No reuse allowed without permission.

spikes was given by an Ornstein–Uhlenbeck process with mean μ_{OU}, volatility σ_{OU} and time constant τ_{OU}, multiplied by a Gaussian gain function representing the neuron position in the receptive field. The input of the PV+ interneurons was the mean of all inputs to its afferent pyramidal cells. The peak mean μ_{OU} was 5000 spikes per second, τ_{OU} was 50 ms and σ_{OU} was $\frac{1}{6}\mu_{OU}\sqrt{2\,\tau_{OU}}$ for the simulations in **Figure 7** and zero everywhere else (i.e. the Poisson rates were constant).

bioRxiv preprint doi: https://doi.org/10.1101/279505; this version posted November 15, 2018. The copyright holder for this preprint (which was not certified by peer review) is the author/funder. All rights reserved. No reuse allowed without permission.

Table 2: model neuron parameters for network modelling

Parameter	FS PV+	Pyramidal	Units
C_m	90	115	pF
k_{low}	14	3.3	nS/mV
k_{high}	1.7	0.1	nS/mV
v_r	-60.6	-65.8	mV
v_{peak}	2.5	22.6	mV
v_t	-43.1	-57	mV
a	0.1	0.0012	ms^{-1}
b	-0.1	3	nS
c	-67	-65.8	mV
d	0.1	10	pA
τ_1^{AMPA}	0.25	0.2	ms
τ_2^{AMPA}	0.77	1.2	ms
τ_1^{GABA}	0.3	0.26	ms
τ_2^{GABA}	2.5	8.5	ms
τ_1^{NMDA}	2	-	ms
τ_2^{NMDA}	60	-	ms
e^{glu}	0	0	mV
e^{GABA}	-70	-70	mV
${\sigma_D}^2$	$0.015/(n_{pyr}^2)$	-	-
C_{syn}	9	-	pF
k^{syn}	$3/n_{pyr}$	-	-
g^{leak}	5	-	nS
e^{leak}	-60.6	-	mV
k^{AMPA}	2^9	-	-
k^{NMDA}	2^{13}	-	-
k^{GABA}	80	80	-
k^{ext}	5	1	-